Ionics (2024) 30:3329–3338
https://doi.org/10.1007/s11581-024-05537-x

RESEARCH

Effect of $MnSO_4$ concentration on the electrochemical performance of β-MnO_2/3D graphene-carbon nanotube hybrids cathode for aqueous zinc-ion batteries

Duolong Jin[1,2] · **Xiaoping Dong**[1,2] · **Shenghai Xin**[1,2] · **Liying Yang**[1,2] · **Jiankai Liu**[1,2] · **Qianran Pang**[1,2]

Received: 7 March 2024 / Revised: 11 April 2024 / Accepted: 14 April 2024 / Published online: 20 April 2024

Abstract

Manganese-based cathode material has a wide range of applications in aqueous zinc-ion batteries, but its structural stability is poor. We can improve the microstructure of manganese-based cathode materials by simple mechanical ball milling methods, thus increasing the discharge capacity of batteries. However, the capacity of manganese-based cathode material batteries decreases rapidly during cycling, which is caused by the dissolution of manganese-based materials in the electrolyte. To ameliorate this problem, in this work, $MnSO_4$ is pre-added to the $ZnSO_4$ electrolyte, which can effectively inhibit the dissolution of the manganese-based material and maintain the conversion reaction inside the battery, providing better cycle life and higher discharge capacity. In addition, with the increase of $MnSO_4$ additive concentration in a certain range, the discharge capacity and cycle life of the batteries were improved (the battery pre-added with 0.5 M $MnSO_4$ solution had the highest reversible specific capacity of up to 521.91 mAh·g^{-1} at a current density of 100 mA·g^{-1} and 109.12 mAh·g^{-1} even at 1 A·g^{-1}, the capacity retention rate remained at 83.8% after cycling for more than 8000 cycles), which provides an idea for the electrolyte regulation of aqueous zinc-ion batteries.

Keywords Aqueous zinc-ion battery · Cathode materials · Electrolyte regulation · Electrochemical

Introduction

Due to the energy scarcity and environmental pollution caused by non-renewable energy sources such as coal and oil, new energy sources are urgently needed to alleviate this pressure [1]. It is well known that lithium-ion batteries have dominated the new energy storage market for many years, but the increasing scarcity of lithium resources, uneven geographic distribution, and the flammability and toxicity of the electrolyte are unfavorable factors that affect the sustainable development of lithium-ion batteries [2, 3]. In contrast, the emergence of mild aqueous ion batteries (potassium, calcium, magnesium, zinc, etc.) has received much attention [4–7], among which aqueous zinc-ion batteries (AZBs) have been favored by researchers due to their environmentally friendly, low-cost, resource-abundant, and high theoretical specific capacity (820 mAh·g^{-1}) advantages [8–10]. The cathode materials play a key role in the overall performance of aqueous zinc-ion batteries. Currently, there are three main types of cathode materials: manganese-based oxides [11–13], vanadium-based oxides [14, 15], and Prussian blue analogs [16, 17]. Manganese-based oxide materials are polycrystalline and have the advantages of low preparation cost, abundant reserves, and simple fabrication, among which manganese dioxide has been recognized as an ideal cathode material for aqueous zinc-ion batteries. However, during the cycling process, manganese-based materials will inevitably lead to the collapse of the electrode structure due to inherent structural defects [18], which in turn affects the capacity and cycling performance of the battery. In a previous study [19], we constructed a hybrid cathode material of β-MnO_2/3D graphene-carbon nanotube cross-links by a simple mechanical ball milling method, which improved the inherent stability of the cathode material, but it still suffers from the problem of faster capacity decay, which depends on

---

✉ Xiaoping Dong
dxp0316@163.com

[1] College of Quality and Technical Supervision of Hebei University, BaoDing 071002, Hebei Province, China

[2] Technology Innovation Center of New Energy Vehicle Power System Lightweighting in Hebei Province (Preparation), BaoDing 071002, Hebei Province, China

the electrolyte modulation to maintain the structural stability during the reaction process.

Cao et al. [20] found excellent electrode performance of MnO_2/nano-graphite flake complexes in $ZnSO_4+MnSO_4$ electrolyte: the discharge capacity reached 230 $mAh\cdot g^{-1}$ at 100 $mA\cdot g^{-1}$, and the capacity retention rate was 80.8% after 1000 cycles at 1 $A\cdot g^{-1}$. Pan et al. [21] added $MnSO_4$ additive to the $ZnSO_4$ electrolyte to regulate the balance of Mn^{2+}, which well suppressed the dissolution of the α-MnO_2 nanofiber cathode, enabling the battery to exhibit excellent multiplicity performance and capacity retention of up to 92% even after 5000 cycles. Soundharrajan et al. [22] established an electrochemical equilibrium between Zn^{2+} and Mn^{2+} in a battery with $ZnMn2O_4$ as the cathode by using 1 M $ZnSO_4$ + 0.1 M $MnSO_4$ electrolyte, which promoted excellent performance. Zhang et al. [23] formulated a $Zn(CF_3SO_3)_2+Mn(CF_3SO_3)_2$ electrolyte, which was able to form a protective porous manganese oxide layer on the surface of the β-MnO_2 cathode, and the battery had 225 $mAh\cdot g^{-1}$ high reversible capacity and long-term recyclability, maintained 94% capacity after 2000 cycles.

Based on this, we can know that the cathode materials formed by Mn-based oxides or mixtures with C mass have excellent electrochemical performance under appropriate electrolyte solution. In this paper, we take the mixture of β-MnO_2/3D graphene-carbon nanotube cross-links (abbreviation: β-MnO_2/3D GPE-CNT) as a target to investigate the effect of the pre-addition of different concentrations of $MnSO_4$ solution (0.1 M, 0.3 M, 0.5 M, 0.6 M) in 2 M $ZnSO_4$ on the electrochemical performance of this cathode material.

Experimental materials and methods

The detailed preparation process of β-MnO_2/3D GPE-CNT is shown in Fig. 1. Before use, the ball milling jar was first cleaned. A mixture of β-MnO_2 powder and 3D graphene-carbon nanotube with a mass ratio of 9:1 was put into the ball milling jar of the high-energy ball mill, as shown in Fig. 1 a, and the mass ratio of stainless steel balls to the mixture was 50:1. The use of several different sizes of stainless steel balls had better ball milling effects. Set the automatic power on and off intervals of 1 min, the total time of 5 h (the actual ball milling process 2.5 h). The obtained β-MnO_2/3D GPE-CNT powders were collected by natural cooling for 1 h after ball milling. The microscopic particle morphology and arrangement of the materials were investigated by field emission scanning electron microscopy (FSEM, S-4800) and transmission electron microscopy (TEM, JEM-F200); the phase structure of the materials was characterized by X-ray diffraction (XRD, SmartLab); and the particle size distribution of the specimens was tested by a laser particle size analyzer (Malvern 3000); The specific surface area of the specimens was tested by a specific surface pore size analyzer (JW-BK200B).

The β-MnO_2/3D GPE-CNT cathode material collected from the above ball milling was mixed with conductive carbon (Super P) and PVDF at the mass ratio of 7:2:1 and put into an onyx mortar to be fully milled, and then dripped into the appropriate amount of N-methyl-2-pyrrolidone (NMP) solution to develop into a slurry. Then the slurry was uniformly coated on the stainless steel foil with a coating machine, and then placed in a vacuum drying oven at 110 °C for 12 h. After drying, the slurry was cut into round positive electrode sheets with a diameter of about 14 mm, and the average mass density of the active substance on the positive electrode sheets was about 0.46 $mg\cdot cm^{-2}$. Then the CR2032 coin batteries were assembled using 2 M $ZnSO_4$ with the addition of 0.1 M, 0.3 M, 0.5 M, and 0.6 M $MnSO_4$ as electrolyte in the order of negative electrode shell, zinc flake, fiberglass diaphragm, positive electrode flake, gasket, and positive electrode shell, respectively. The assembled batteries were allowed to stand for more than 6 h; galvanostatic charge–discharge (GCD) tests were performed in a Neware battery test system. The multiplicity performance and cycle life of the batteries under different electrolytes were tested at different current densities in the range of 100 $mA\cdot g^{-1}$ to 1 $A\cdot g^{-1}$ under a voltage window of 1.0 ~ 1.8 V, respectively

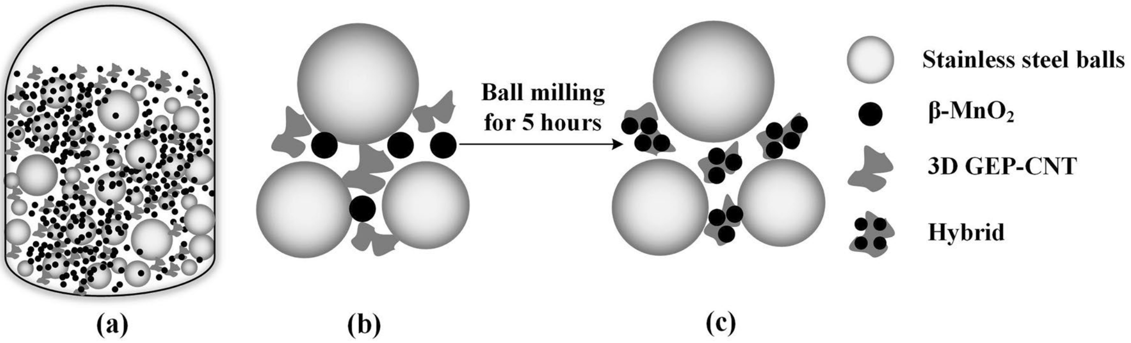

Fig. 1 Schematic diagram of the preparation of β-MnO_2/3D GPE-CNT by high-energy ball milling

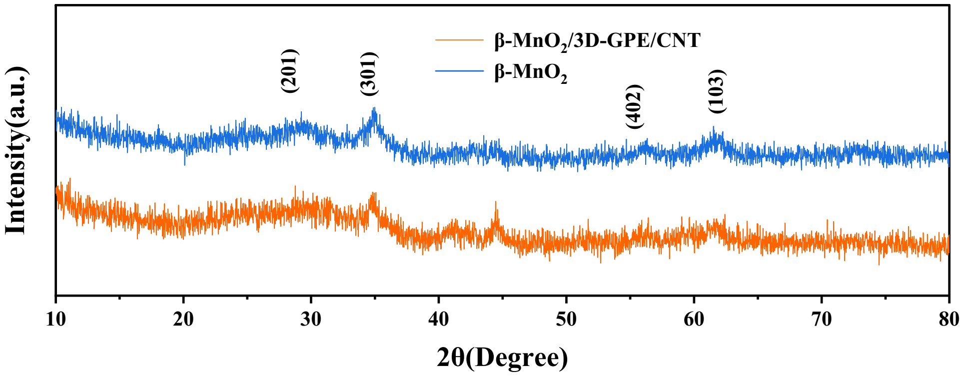

Fig. 2 XRD patterns of hybridized materials and β-MnO$_2$

(BTS, CT-4008, Neware). Cyclic voltammetry (CV) curves were tested in the voltage range of 0.8 ~ 1.8 V at a scan rate of 0.1 ~ 0.5 mv·s^{-1} on a CHI660E electrochemical workstation, and electrochemical impedance spectroscopy (EIS) analysis was performed in the frequency range of 0.01 Hz ~ 10 kHz.

Results and discussion

Micro-morphology and analysis

The XRD patterns of the original sample of β-MnO$_2$ as well as the β-MnO$_2$/3D GPE-CNT hybrids are shown in Fig. 2. It can be seen that the XRD patterns related to MnO$_2$ match the standard card (JCPDS: 39–0375) of the original sample of β-MnO$_2$, and there are obvious diffraction peaks at 2θ = 29.31°, 35.02°, 56.21°, and 61.54°, corresponding to the (201), (103), (402), and (103) facets, respectively, which indicates that ball milling before and after does not significantly change the phase structure of the samples [19].

The microstructures of pure β-MnO$_2$ and β-MnO$_2$/3D GPE-CNT hybrids were measured by SEM and TEM, and the results are shown in Fig. 3. As can be seen in Fig. 3 a and b, the pure β-MnO$_2$ samples exhibit a tightly packed appearance with an angular blocky particle structure. The ball-milled hybrids, on the other hand, showed a distribution of spherical particles, and the agglomeration phenomenon was obviously reduced. In addition, under the same magnification, the SEM images of the ball-milled β-MnO$_2$/3D GPE-CNT hybrids observed significantly more particles, which indicated that ball milling greatly reduced the particle

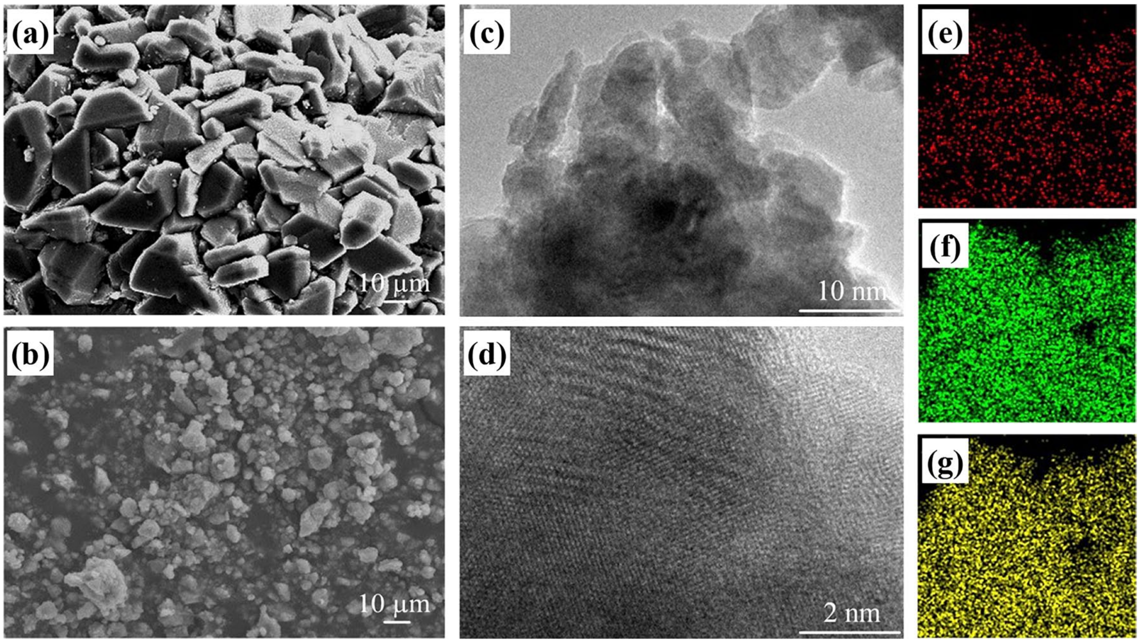

Fig. 3 Micro-morphological analysis diagrams. a SEM images of β-MnO$_2$; b SEM images of β-MnO$_2$/3D GPE-CNT hybrids; c, d TEM images of hybrids after ball milling; e–g the distribution of C, O, and Mn elements in the hybrids, respectively

size of the cathode material. This would lead to an increase in the specific surface area of the material a better contact reaction with the electrolyte [25], which can be verified in the next experiment. Figure 3 c shows the TEM image of the β-MnO_2/3D GPE-CNT hybrids, which shows that the 3D GPE-CNT and β-MnO_2 form a whole, and the β-MnO_2 particles are more dispersed to cover the surface of the 3D network [20]. The atomic arrangement in Fig. 3 d shows that a few lattice distortions appeared after ball milling, which are defects caused by collision and extrusion during the ball milling process. Figure 3 e–g can further show that the elements C, O, and Mn are more uniformly distributed in the hybrids, which further proves the uniformly dispersed distribution of β-MnO_2 after ball milling.

Further specific surface area analysis of pure β-MnO_2 and β-MnO_2/3D GPE-CNT hybrids yielded results of 14.24 $m^2 \cdot g^{-1}$ and 22.38 $m^2 \cdot g^{-1}$, respectively, and the particle size distribution of the specimens was tested using a laser particle size analyzer, with an average particle size of 20.33 μm, which is in line with the phenomenon observed above in the experimental results.

Electrochemical performance and analysis

Figure 4 a shows the capacity decay curves of the cells with different concentrations of $MnSO_4$ solution pre-added to the electrolyte at 100 $mA \cdot g^{-1}$. The discharge specific capacity of the β-MnO_2/3D GPE-CNT cathode material with 2 M $ZnSO_4$ + 0.1 M $MnSO_4$ solution as the electrolyte reaches 221.91 $mAh \cdot g^{-1}$ after full activation is higher than the specific capacity when $ZnSO_4$ solution is used as electrolyte alone, and the capacity of the batteries with $MnSO_4$ solution added decreases very slowly after the batteries are stabilized. This indicates that the capacity decay of the battery can be well suppressed after adding $MnSO_4$ in the electrolyte. This is because the dissolution of the cathode material can be effectively inhibited by pre-adding appropriate metal cations to the solution according to the chemical dissolution-equilibrium principle of the cathode material and the active substance in the electrolyte, so pre-adding $MnSO_4$ to the $ZnSO_4$ electrolyte can inhibit the dissolution of MnO_2 by establishing the dissolution equilibrium of Mn^{2+} in the electrolyte and cathode materials. This principle was confirmed by Pan [21] et al. They examined the concentration of Mn^{2+} in the electrolyte by technical device and found that the concentration of Mn^{2+} in the $ZnSO_4$ electrolyte was directly proportional to the rate of capacity decay of the batteries, which indicated that the capacity decay was due to the dissolution of the anode MnO_2 in the electrolyte, and when the capacity was stabilized, the concentration of Mn^{2+} was relatively stable, which was due to the fact that the concentration of Mn^{2+} in the electrolyte has reached equilibrium with the dissolution of anode MnO_2, which inhibits the dissolution of the anode material.

Continuing to increase the concentration of $MnSO_4$ solution in the electrolyte to 0.3 M, it can be seen from the constant-current GCD curve shown in Fig. 4 a that the maximum discharge specific capacity of the battery after activation reached 365.76 $mAh \cdot g^{-1}$, and the capacity retention rate was also improved very well, which indicates that increasing the concentration of Mn^{2+} can not only deepen the internal chemical reaction of the battery, but also better inhibit the dissolution of cathode material in the electrolyte, effectively slowing down the capacity degradation of the battery [23]. This is shown until the concentration of $MnSO_4$ solution is increased to 0.5 M. Under this condition, the specific capacity of the battery rises rapidly after more than ten turns of full activation, and reaches an astonishing 521.91 $mAh \cdot g^{-1}$ after 27 turns of cyclic charging and discharging, which is much higher than what is reported in related literatures [20, 24, 25]. The capacity can be well maintained after the battery is stabilized. After 100 turns of constant current charging and discharging, the discharge specific capacity is maintained at 416.48 $mAh \cdot g^{-1}$. However, when the concentration of $MnSO_4$ solution is increased to 0.6 M, the capacity of the battery does not have a rapid and substantial increase in the process of activation as that of 0.5 M, but instead, it exhibits a similar nature of capacity decay as that of 0.3 M. This can be verified from the relevant studies [21, 23, 27]: appropriate concentration of $MnSO_4$ added to the electrolyte can effectively inhibit the collapse of the anode MnO_2 structure due to the dissolution of anode materials in the electrolyte to participate in the reaction, thus improving the specific capacity of discharge as well as the capacity retention rate, but the concentration of $MnSO_4$ in the electrolyte is too high which will not be conducive to the participation of the anode materials in the reaction. Figure 4 b shows the charge–discharge curves of batteries with different $MnSO_4$ concentrations as electrolyte when the specific capacity reaches the highest value at 100 $mA \cdot g^{-1}$, and it can be seen that the discharge curves have inflection points at about 1.4 V and 1.3 V. With the increase of the $MnSO_4$ concentration in the electrolyte, the discharge platforms at 1.4 V and 1.3 V become more obvious, and the consistency of the shapes of the discharge curves is better, which show the good stability of the battery. The Coulomb efficiency is above 96%, showing high reversibility.

The charging and discharging curves of the battery at different current densities when the electrolyte is 2 M $ZnSO_4$ + 0.5 M $MnSO_4$ solution are shown in Fig. 4 c. The contribution of the voltage range below 1.3 V to the capacity decreases as the current density increases, and this section reacts more slowly and is the main capacity contributing stage. The discharge specific capacity of the battery reaches 432.33 $mAh \cdot g^{-1}$ at 200 $mA \cdot g^{-1}$ and 316.75 $mAh \cdot g^{-1}$ at

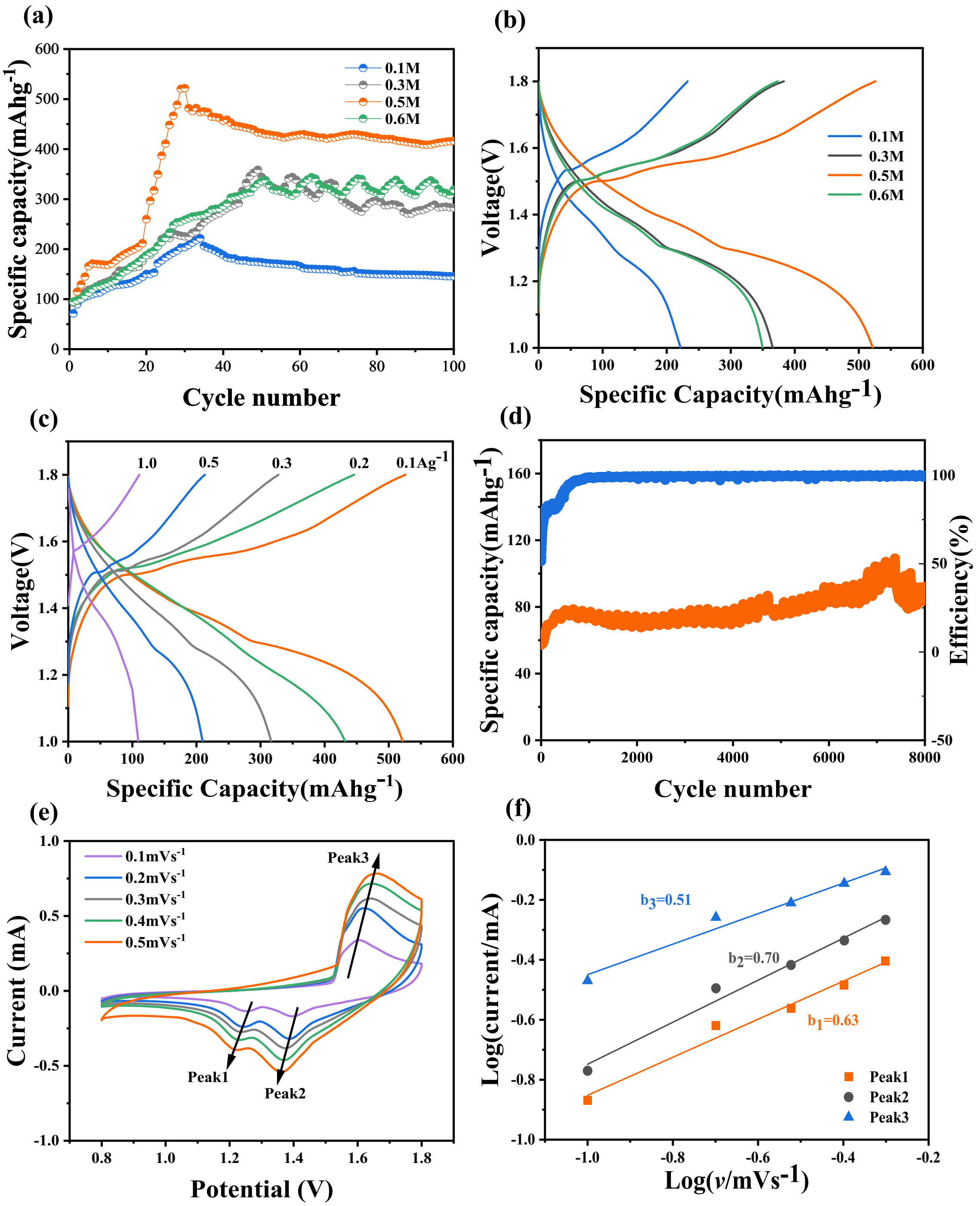

Fig. 4 **a** Capacity decay curves at 100 mA·g^{-1} with the addition of different concentrations of MnSO$_4$; **b** charge–discharge curves when the specific capacity reaches the maximum; **c** charge–discharge curves when the electrolyte is 2 M ZnSO$_4$ + 0.5 M MnSO$_4$; **d** cycling performance at 1A·g^{-1} when the electrolyte is 2 M ZnSO$_4$ + 0.5 M MnSO$_4$ at 1A·g^{-1} cycling performance; **e** CV curves with the addition of 0.5 M MnSO$_4$; **f** Tafel curves fitting the peaks in **e**

300 mA·g^{-1}, and 209.55 mAh·g^{-1} even at 500 mA·g^{-1} current density. The results show that the batteries with 0.5 M MnSO$_4$ solution as electrolyte additive have excellent multiplication performance. To further investigate the cycling stability of the batteries, the batteries were charged and discharged cyclically at a high current density of 1 A·g^{-1}; as shown in Fig. 4 d, the discharge specific capacity of the batteries reached about 80 mAh·g^{-1} after full activation. The overall trend of the battery capacity in the subsequent cycles showed a slow oscillation, and there was no obvious

attenuation until 7377 cycles. On the contrary, the discharge specific capacity of the battery increased before 7377, reached a maximum of 109.12 $mAh \cdot g^{-1}$ at 7377 cycles, the discharge specific capacity decayed only after 7377 cycles. Overall, the batteries with β-MnO_2/3D GPE-CNT as cathode have excellent cycling stability and capacity retention when 0.5 M $MnSO_4$ solution is added to the electrolyte, with a high discharge specific capacity of up to 109.12 $mAh \cdot g^{-1}$ even at a high current density of 1 $A \cdot g^{-1}$. After 8000 cycles of charging and discharging, the specific capacity is still 91.49 $mAh \cdot g^{-1}$, which is 83.8% of the highest discharge specific capacity.

The electrochemical performance of β-MnO_2/3D GPE-CNT batteries at 0.5 M $MnSO_4$ as an electrolyte additive was further investigated using CV curves, as shown in Fig. 4 e, which were obtained at different scanning rates (0.1–0.5 $mv \cdot s^{-1}$) in the potential range of 0.8–1.8 V. The CV curves showed two distinct reduction peaks at 1.25 V and 1.39 V (peak 1, peak 2), which are related to the conversion reaction (Mn^{4+}/Mn^{2+} two-electron reaction) and the insertion of Zn^{2+}, respectively [28]. The oxidation peak (peak 3) is related to the extraction of Zn^{2+} [26]. With the increase of scanning rate, the CV curves can keep similar shapes, indicating that the anode materials have good reversibility. And with the increase of scanning frequency, the peak currents of the peaks gradually increase, and the potentials of peak 1 and peak 2 move to the low-voltage direction, while the potential of peak 3 moves to the high-voltage direction. The electrochemical kinetics of these cathodes at different scan rates can be determined by Eqs. (1) and (2) [29]:

$$i = av^b \tag{1}$$

$$lg(i) = blg(v) + lg(a) \tag{2}$$

where a and b are variable parameters obtained from the slope of lg(v)-lg(i), which indicates the dominance of diffusive processes when b is approximately equal to 0.5 and capacitive behavior when b is approximately 1 [25]. i denotes the peak current and v is the scanning rate. As can be seen from Fig. 4 f, the parameters b for peaks 1–3 are 0.63, 0.70, and 0.51, respectively, which are all closer to 0.5, confirming that both the insertion/extraction and transformation reactions of Zn^{2+} are controlled by diffusion.

As shown in Fig. 5 a, b, and c, the CV curves are given when 0.1 M $MnSO_4$, 0.3 M $MnSO_4$, and 0.6 M $MnSO_4$ are used as electrolyte additives, respectively. After analyzing and calculating, the Tafel slopes of each peak of the CV curves are still close to 0.5 at this time, which again proves that the electrochemical behavior of the batteries is also dominated by diffusion. Next, the CV curves of electrolyte additives with different concentrations of $MnSO_4$ were compared at the same scanning frequency, and Fig. 5 d gives the CV curves of electrolyte additives of 0.1 M $MnSO_4$, 0.3 M $MnSO_4$, and 0.5 M $MnSO_4$ at a scanning frequency of 0.1 mv/s. The absolute areas of the closed CV curves were analyzed using Origin software, and we normalized the obtained data to show that the areas of the CV curves for electrolytes with 0.1 M $MnSO_4$, 0.3 M $MnSO_4$, and 0.5 M $MnSO_4$ were 9.03, 10.45, and 13.78, respectively. It can be clearly seen that as the concentration of $MnSO_4$ in the electrolyte increases from 0.1 to 0.5 M, the area wrapped by the CV curve and the ratio of peak current gradually increases, which is consistent with the previous performance of the discharge specific capacity of the batteries with different concentrations of $MnSO_4$ additives. The batteries have the highest discharge specific capacity with the addition of 0.5 M $MnSO_4$, and therefore the area wrapped by the CV curve and the peak current are also the maximum. Also in Fig. 5 d, it can be seen that as the concentration of $MnSO_4$ in the electrolyte increases from 0.1 to 0.5 M, peak 1 of the CV curve is shifted to the left and peak 2 is shifted to the right, and the potentials of the reduction peaks of the CV curves (peak 1 and peak 2) corresponding to the addition of 0.1 M $MnSO_4$ as an additive to the electrolyte are 1.26 V and 1.38 V, respectively. Compared to 1.25 V and 1.39 V for 0.5 M $MnSO_4$, it indicates that the electrolyte at low concentration of $MnSO_4$ addition is unfavorable for Zn^{2+} insertion reaction, but instead, it is favorable for the conversion reaction. Since the conversion reaction consumes MnOOH to produce by-products, this will in turn be detrimental to the H^+ insertion reaction and limit the discharge performance of the batteries. One explanation is that low concentrations of $MnSO_4$ are unfavorable for H^+ insertion, which is mainly affected by the pH value [26], the pH of 2 M $ZnSO_4$ + 0.1 M $MnSO_4$ solution is about 4, while that of 2 M $ZnSO_4$ + 0.5 M $MnSO_4$ solution is about 3; acidic conditions are more favorable for the formation of a two-electron (Zn^{2+} and H^+) insertion mechanism, which provides a higher reversible specific capacity. Further analyzing this figure, we can see that the peak current of the reduction peak 1 increases dramatically during the increase of the $MnSO_4$ concentration in the electrolyte from 0.1 to 0.5 M, which well illustrates that the contribution of the conversion reaction to the discharge capacity of the batteries is significantly higher, and that the degree of conversion of MnO_2 to $Mn2^+$ is deeper. This can be verified from Fig. 4 b, where we calculated the proportion of the discharge capacity of the discharge stage corresponding to the conversion reaction (peak 1) (about 1.3 V or less) to the total capacity, and it can be obtained that the capacity contribution of the conversion reaction rises from 36 to 45% in the process of increasing the $MnSO_4$ concentration in the electrolyte from 0.1 to 0.5 M, which is in agreement with the test of the CV curve results.

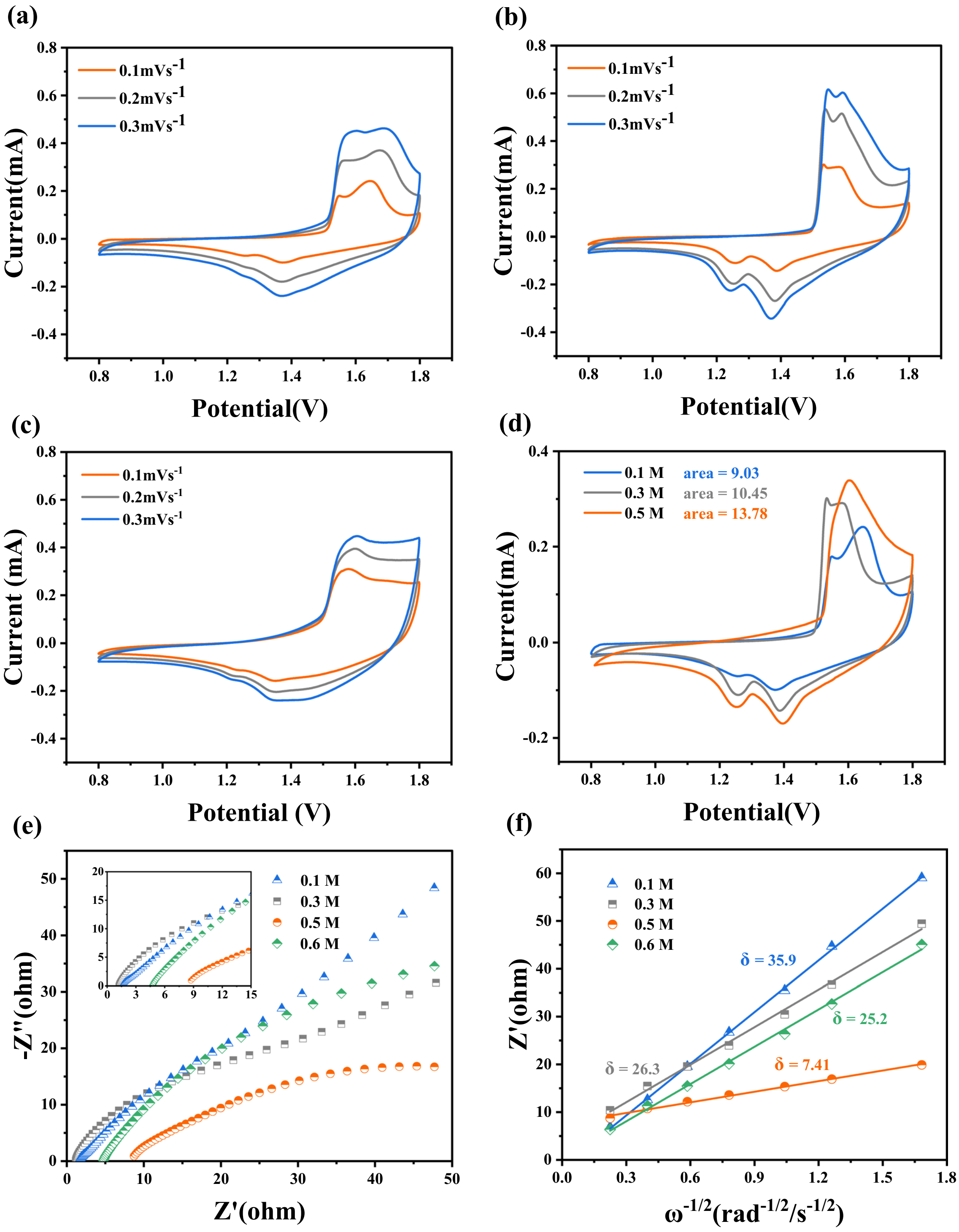

Fig. 5 **a** CV curves with the addition of 0.1 M $MnSO_4$; b CV curves with the addition of 0.3 M $MnSO_4$; **c** CV curves with the addition of 0.6 M $MnSO_4$; **d** CV curves with the addition of different concentrations of $MnSO_4$ for a scanning frequency of 0.1 mv·s^{-1}; **e** EIS Nyquist curves with different concentrations of $MnSO_4$; **f** fitted Warburg slope plots

Then the CV curves of Fig. 5 d were further refined, and it was found that a small oxidation peak appears to the left of the peak 3 oxidation peak at low concentrations of $MnSO_4$ added to the electrolyte, which corresponds to the inverse process of the conversion reaction [26], suggesting that the Mn^{2+} in the electrolyte produces by-products to attach to the surface of the cathode material. When the $MnSO_4$ concentration was increased from 0.5 M, this small oxidation peak was no longer obvious, which further proved that the conversion reaction basically proceeded in the positive direction and the two-electron conversion mechanism (Mn^{4+}/Mn^{2+}) deepened at the concentration of 0.5 M $MnSO_4$, which provided the batteries with higher reversible specific capacity and cycle life.

The EIS-fitted Nyquist curves of the batteries in the frequency range of 0.01 Hz ~ 10 kHz for different concentrations of $MnSO_4$ solution as electrolyte additive are given in Fig. 5 d. Among them, the bulk-phase ion diffusion coefficient (D_{ion}) is an important parameter affecting the dynamic performance of zinc-ion batteries with the following equation:

$$D_{\text{ion}} = \frac{R^2T^2}{2n^4A^2{C_{ion}}^2\sigma^2} \tag{3}$$

where R is the gas constant, T is the operating temperature of the batteries (298.15 K), n is the number of electrons transferred in each molecule, F is Faraday's constant, A is the area of the electrode (1.54 cm^2), and C_{ion} is the concentration of ions in the active substance [30]. The bulk-phase ionic diffusion coefficient of Zn^{2+} in different electrolytes (DZn^{2+}) can be Warburg factor (σ) determined, σ being the slope of the Z'-$\omega^{-1/2}$ curve, which can be obtained from the results of the fit in Fig. 5 f. After calculation, the DZn^{2+} in the electrolyte at the content of 0.1 M $MnSO_4$ and 0.5 M $MnSO_4$ are 1.45×10^{-12} $cm^2\cdot s^{-1}$ and 2.74×10^{-12} $cm^2\cdot s^{-1}$, respectively, which again illustrates that 2 M $ZnSO_4$ + 0.5 M $MnSO_4$ has a higher ion diffusion rate when used as an electrolyte, which is a great advantage for the improvement of discharge capacity. In addition, the excellent rate performance and cycling stability are inextricably linked to the chemical structure of the selected cathode materials [19]: (1) The layered structure of β-MnO_2 is more favorable for the insertion of M^+ and Zn^{2+} and the transfer of Mn^{2+} [31]; (2) the active sites of β-MnO_2 particles attached to the β-MnO_2/3D GPE-CNT hybrid after ball milling are more easily contacted with the electrolyte; (3) ball milling significantly reduces the particle size of β-MnO_2 particles, which results in an increase in the specific surface area and an acceleration of the ion diffusion rate; (4) the generation of new chemical bonds enhanced the internal stability and interfacial adhesion of the hybrids; (5) the excellent electrical conductivity of graphene enhanced the conductivity of the cathode material, which in turn increased the charge transfer rate.

Combined with the electrochemical performance and capacity decay analysis, the β-MnO_2/3D GPE-CNT aqueous zinc-ion batteries with $MnSO_4$ additives in the electrolyte are consistent with the reaction mechanism for the coexistence of the H^+, Zn^{2+} co-insertion/extraction, and the conversion reactions. The reaction principle are described as follows:

Cathode

$$MnO_2 + H^+ + e^- \leftrightarrow MnOOH \tag{4}$$

$$2e^- + 2MnO_2 + Zn^{2+} \leftrightarrow ZnMn_2O_4 \tag{5}$$

$$MnO_2 + 2e^- + 4H^+ \leftrightarrow Mn^{2+} + 2H_2O \tag{6}$$

Anode

$$Zn - 2e^- \leftrightarrow Zn^{2+} \tag{7}$$

where Eqs. (4) and (5) correspond to the insertion reactions of H^+ and Zn^{2+}, respectively. The products produced by the reactions of Eqs. (4) and (5) do not exist stably, which will react with ${SO_4}^{2-}$ and H_2O in solution to produce by-products [24, 26]. Equation (6) can be understood as a conversion reaction equation that ignores the intermediate by-product production process, with the end result that anodic MnO_2 is reduced to divalent Mn^{2+}, providing higher discharge specific capacity. In fact, in order to obtain the direct conversion of MnO_2/Mn^{2+}, efforts have been made by many scholars, and most of them have proved that most of this direct conversion reacts only under high high-voltage state in acidic electrolyte [32–34], whereas this conversion is accompanied by the generation of by-products in the low-voltage state [26, 35, 36]. Therefore, if the direct conversion of MnO_2/Mn^{2+} can be fully realized, the reversible specific capacity of the aqueous zinc-ion batteries will be increased to a much more appreciable magnitude. In addition, the $MnSO_4$ additive in the electrolyte will help to maintain the reversibility of the conversion reaction, and effectively inhibit the structural collapse brought about by the dissolution of the anode MnO_2 while ensuring the high discharge capacity brought about by the conversion reaction, so as to improve the stability of the cycle, which also explains why the β-MnO_2/3D GPE-CNT batteries with 2 M $ZnSO_4$ + 0.5 M $MnSO_4$ as electrolyte have a 521.91 $mAh\cdot g^{-1}$ high discharge specific capacity and ultra 8000 turns long cycle life.

Conclusion

In summary, in this paper, β-MnO_2/3D GPE-CNT were prepared by a simple and environmentally friendly ball milling method, and the nature of low crystallinity and particle size reduction greatly reduced the agglomeration phenomenon of the original β-MnO_2 samples. This enhances the specific surface area of the cathode material, and the contact between the electrolyte and the cathode material is more adequate, which is correspondingly more favorable to the improvement of the Zn^{2+} diffusion rate. The excellent performance of this β-MnO_2/3D GPE-CNT cathode material is one of the important reasons for the formation of the two-electron conversion mechanism. This two-electron conversion mechanism has a high theoretical specific capacity of 616 mAh·g^{-1} when the theoretical specific capacity is only 308 mAh·g^{-1} for the one-electron reaction pair (Mn^{4+}/Mn^{3+}). In addition, the relationship between the pre-addition of different concentrations of $MnSO_4$ to the electrolyte and the discharge capacity as well as the cycling performance of the batteries was investigated, and the reaction mechanism of the cathode of the batteries was investigated by combining the analytical means of XRD, SEM, TEM, CV, EIS, etc. The results showed that Mn^{2+} in the electrolyte could not only effectively inhibit the dissolution of the anode manganese-based material, but also its concentration had a great influence on the maintenance of the Mn^{4+}/Mn^{2+} conversion pathway. The batteries with the pre-addition of 0.5 M $MnSO_4$ solution had a specific capacity of 521.91 mAh·g^{-1} at 100 mA·g^{-1} and 109.12 mAh·g^{-1} at 1A·g^{-1}, and the capacity retention rate remained 83.8% after more than 8000 cycles. This provided an idea for the regulation of the electrolyte in Zn–Mn aqueous zinc-ion battery.

Author contributions Duolong Jin (First Author): Data Curation, Methodology, Investigation, Formal Analysis, Writing-Original Draft; Xiaoping Dong (Corresponding Author): Conceptualization, Funding Acquisition, Resources, Supervision, Writing-Review & Editing. Shenghai Xin: Visualization, Investigation; Liying Yang: Resources, Supervision; JianKai Liu: Validation; Data Curation Qianran Pang: Visualization; All authors reviewed the manuscript.

Funding This study received financial supports from the Natural Science Foundation of Hebei Province, China, (E2021201032); 2023 Hebei Province and Hebei University School-level Student Innovation and Entrepreneurship Training project (S202310075044 and 2023232); Ministry of Education's "Spring Fai Project" cooperative research project (202200397); and Hebei University 2022 Laboratory Opening Project (sy202266).

Data availability No datasets were generated or analysed during the current study.

Declarations

Competing interests The authors declare no competing interests.

References

1. Pasta M, Wessells CD, Cui Y et al (2012) A high-rate and long cycle life aqueous electrolyte battery for grid-scale energy storage. Nat Commun 3:1149. https://doi.org/10.1038/ncomms2139
2. Li M, Lu J, Chen Z et al (2018) 30 years of lithium-ion batteries. Adv Mater 33:1800561. https://doi.org/10.1002/adma.201800561
3. Liu X, Ren D, Su H et al (2018) Thermal runaway of lithium-ion batteries without internal short circuit. Joule 10:2047–2064. https://doi.org/10.1016/j.joule.2018.06.015
4. Wei X, Wei J, Song Y et al (2021) Potassium mediated Co-Fe-based Prussian blue analogue architectures for aqueous potassium-ion storage. Chem Commun 57:7019–7022. https://doi.org/10.1039/d1cc01852c
5. Wang M, Yagi S (2020) Layered birnessite MnO_2 with enlarged interlayer spacing for fast Mg-ion storage. J Alloy Compd 820:153135. https://doi.org/10.1016/j.jallcom.2019.153135
6. Cang R, Zhao C, Ye K et al (2020) Aqueous calcium-ion battery based on a mesoporous organic anode and a manganite cathode with long cycling performance. Chemsuschem 13:3911–3918. https://doi.org/10.1002/cssc.202000812
7. Fang GZ, Zhou J, Pan A et al (2018) Recent advances in aqueous zinc-ion batteries. ACS Energy Lett 3:2480–2501. https://doi.org/10.1021/acsenergylett.8b01426
8. Zhang K, Han X, Hu Z, Zhang X, Tao Z, Chen J (2015) Nanostructured Mn-based oxides for electrochemical energy storage and conversion. Chem Soc Rev 44:699–728. https://doi.org/10.1039/c4cs00218k
9. Wang J, Yang Y, Zhang Y, Li Y, Sun R, Wang Z, Wang H (2021) Strategies towards the challenges of zinc metal anode in rechargeable aqueous zinc ion batteries. Energy Storage Mater 35:19–46. https://doi.org/10.1016/j.ensm.2020.10.027
10. Konarov N, Voronina JH, Jo Z, Bakenov YK, Sun ST (2018) Myung Present and future perspective on electrode materials for rechargeable zinc-ion batteries. ACS Energy Lett 3:2620–2640. https://doi.org/10.1021/acsenergylett.8b01552
11 Guo C, Liu H, Li J et al (2019) Ultrathin delta-MnO_2 nanosheets as cathode for aqueous rechargeable zinc ion battery. Electrochim Acta 304:370–377. https://doi.org/10.1016/j.electacta.2019.03.008
12. Jiang B, Xu C, Wu C et al (2017) Manganese sesquioxide as cathode material for multivalent zinc ion battery with high capacity and long cycle life. Electrochim Acta 229:422–428. https://doi.org/10.1016/j.electacta.2017.01.163
13. H Chen, W Zhou, Zhu D et al (2020) Porous cube-like Mn_3O_4@C as an advanced cathode for low-cost neutral zinc-ion battery. J Alloys Compd 813. https://doi.org/10.1016/j.jallcom.2019.151812
14. Hu P, Yan M, Zhu T et al (2017) Zn/V_2O_5 aqueous hybrid-ion battery with high voltage platform and long cycle life. ACS Appl Mater Interfaces 9:42717–42722. https://doi.org/10.1021/acsami.7b13110
15. Zhang N, Jia M, Dong Y et al (2019) Hydrated layered vanadium oxide as a highly reversible cathode for rechargeable aqueous zinc batteries. Adv Func Mater 29:1807331. https://doi.org/10.1002/adfm.201807331
16. Jia Z, Wang B, Wang Y (2015) Copper hexacyanoferrate with a well-defined open framework as a positive electrode for aqueous zinc ion batteries. Mater Chem Phys 14:601–606. https://doi.org/10.1016/j.matchemphys.2014.11.014
17 Zhang L, Chen L, Zhou X et al (2015) Towards high-voltage aqueous metal-ion batteries beyond 1.5 V: the zinc/zinc hexacyanoferrate system. Adv Energy Mater 5:1400930. https://doi.org/10.1002/aenm.201400930
18. Wang J, Wang JG, Liu H, Wei C, Kang F (2019) Zinc ion stabilized MnO_2 nanospheres for high capacity and long lifespan aqueous zinc-ion batteries. J Mater Chem A 7:13727. https://doi.org/10.1039/c9ta03541a
19. Xin SH, Dong XP, Jin DL, Yang LY, Su DD (2023) β-MnO_2/three-dimensional graphene-carbon nanotube hybrids as cathode for aqueous zinc-ion battery. J Alloy Compd 968:172115. https://doi.org/10.1016/j.jallcom.2023.172115
20. Cao J, Zhang DD, Zhang XY, Wang SM, Han JT, Zhao YS, Huang YH, Qin JQ (2020) Mechanochemical reactions of MnO_2 and graphite nanosheets as a durable zinc ion battery cathode. Appl Surface Sci 534(1–12):147630. https://doi.org/10.1016/j.apsusc.2020.147630

21. Pan H, Shao Y, Yan P et al (2016) Reversible aqueous zinc/manganese oxide energy storage from conversion reactions. Nat Energy 1:16039. https://doi.org/10.1038/nenergy.2016.39
22. Soundharrajan V, Sambandam B, Kim S, Islam S, Jo J et al (2020) The dominant role of Mn^{2+} additive on the electrochemical reaction in $ZnMn_2O_4$ cathode for aqueous zinc-ion batteries. Energy Storage Mater 28:407–417. https://doi.org/10.1016/j.ensm.2019.12.021
23. Zhang N, Cheng F, Liu J et al (2017) Rechargeable aqueous zinc-manganese dioxide batteries with high energy and power densities. Nat C 405. https://doi.org/10.1038/s41467-017-00467-x
24. Zhao S, Han B, Zhang DT et al (2018) Unravelling the reaction chemistry and degradation mechanism in aqueous Zn/MnO_2 rechargeable batteries. J Mater Chem A 6:5733–5739. https://doi.org/10.1039/c8ta01031e
25. Jiang W, Xu X, Liu Y, Tan L et al (2020) Facile plasma treated β-MnO_2@C hybrids for durable cycling cathodes in aqueous Zn-ion batteries. J Alloy Compd 827:154273. https://doi.org/10.1016/j.jallcom.2020.154273
26. Li GZ, Huang ZX, Chen J et al (2020) Rechargeable Zn-ion batteries with high power and energy densities: a two-electron reaction pathway in birnessite MnO_2 cathode materials. J Mater Chem A 8:1966–1974. https://doi.org/10.1039/c9ta11985j
27. Chamoun M, Brant WR, Tai C et al (2018) Rechargeability of aqueous sulfate Zn/MnO_2 batteries enhanced by accessible Mn^{2+} ions. Energy Storage Mater 15:351–360. https://doi.org/10.1016/j.ensm.2018.06.019
28. Cao J, Zhang D, Zhang X et al (2020) A universal and facile approach to suppress dendrite formation for Zn and Li metal anode. J Mater Chem A 8:9331–9344. https://doi.org/10.1039/d0ta02486d
29. Brezesinski T, Wang J, Tolbert SH et al (2010) Ordered mesoporous α-MoO_3 with iso oriented nanocrystalline walls for thin-film pseudocapacitors. Nat Mater 9:146–151. https://doi.org/10.1038/nmat2612
30. Liu M, Zhao Q, Liu H, Yang J et al (2019) Tuning phase evolution of β-MnO_2 during microwave hydrothermal synthesis for high-performance aqueous Zn ion battery. Nano Energy 64:103942. https://doi.org/10.1016/j.nanoen.2019.103942
31. Zhu CY, Li PZ, Xu GY, Cheng H, Gao G (2023) Recent progress and challenges of Zn anode modification materials in aqueous Zn-ion batteries. Coord Chem Rev 485:215142. https://doi.org/10.1016/j.ccr.2023.215142
32. Yang M, Chen R, Shen Y et al (2020) A high-energy aqueous manganese-metal hydride hybrid battery. Adv Mater 32:e2001106. https://doi.org/10.1002/adma.202001106
33. Zhang Y, Li M, Li H et al (2023) Catholyte modulation and Prussian blue/Berlin green redox mediator enabling efficient high-potential Mn^{2+}/MnO_2 reaction for aqueous hybrid batteries. Small Structures 5:2300257. https://doi.org/10.1002/sstr.202300257
34. Chao D, Zhou W, Ye C et al (2019) An electrolytic Zn-MnO_2 battery for high-voltage and scalable energy storage. Angew Chem Int Ed 58:7823–7828. https://doi.org/10.1002/anie.201904174
35. Zeng XH, Liu JT, Mao JF et al (2020) Toward a reversible Mn^{4+}/Mn^{2+} redox reaction and dendrite-free Zn anode in near-neutral aqueous Zn/MnO_2batteries via salt anion chemistry. Adv Energy Mater 10:1904163. https://doi.org/10.1002/aenm.201904163
36. Zhong ZP, Li JY, Li LY et al (2022) Improving performance of zinc-manganese battery via efficient deposition/dissolution chemistry. Energy Storage Mater 46:165–174. https://doi.org/10.1016/j.ensm.2022.01.006